Materials Today Bio 21 (2023) 100714

Contents lists available at ScienceDirect

Materials Today Bio

journal homepage: www.journals.elsevier.com/materials-today-bio

Control of blood capillary networks and holes in blood-brain barrier models by regulating elastic modulus of scaffolds

Yucheng Shang [a], Marie Piantino [a], Jinfeng Zeng [a,b], Fiona Louis [a,c], Zhengtian Xie [a], Tomomi Furihata [d], Michiya Matsusaki [a,c,*]

[a] Department of Applied Chemistry, Graduate School of Engineering, Osaka University, Suita, Osaka, Japan
[b] Research Fellow of Japan Society for the Promotion of Science, Kojimachi Business Center Building, Kojimachi, Tokyo, Japan
[c] Joint Research Laboratory (TOPPAN INC.) for Advanced Cell Regulatory Chemistry, Osaka University, Suita, Osaka, Japan
[d] School of Pharmacy, Tokyo University of Pharmacy and Life Sciences, Hachioji, Tokyo, Japan

ARTICLE INFO

Keywords:
Tissue engineering
Elastic modulus
Blood-brain barrier model
Blood capillary network
Blood capillary hole

ABSTRACT

The blood-brain barrier (BBB) is a type of capillary network characterized by a highly selective barrier, which restricts the transport of substances between the blood and nervous system. Numerous *in vitro* models of the BBB have been developed for drug testing, but a BBB model with controllable capillary structures remains a major challenge. In this study, we report for the first time a unique method of controlling the blood capillary networks and characteristic holes formation in a BBB model by varying the elastic modulus of a three-dimensional scaffold. The characteristic hole structures are formed by the migration of endothelial cells from the model surface to the interior, which have functions of connecting the model interior to the external environment. The hole depth increased, as the elastic modulus of the fibrin gel scaffold increased, and the internal capillary network length increased with decreasing elastic modulus. Besides, internal astrocytes and pericytes were also found to be important for inducing hole formation from the model surface. Furthermore, RNA sequencing indicated up-regulated genes related to matrix metalloproteinases and angiogenesis, suggesting a relationship between enzymatic degradation of the scaffolds and hole formation. The findings of this study introduce a new method of fabricating complex BBB models for drug assessment.

1. Introduction

Tissue engineering is a multidisciplinary field that combines engineering, materials and biological sciences and was initially focused on the repair or replacement of damaged tissues. Compared to traditional two-dimensional (2D) cell culture, three-dimensional (3D) cell culture models developed by tissue engineering have greater physiological relevance [1]. 3D *in vitro* capillary network models began to offer promising solutions for the treatment of a wide range of diseases due to their ability to form complex structures similar to *in vivo* tissues and mimic the physiological environment of natural cellular microvasculature. Their ability to form much more complex structures and their facility to mimic the microenvironment of natural cellular microvasculature [2,3]. Therefore, the *in vitro* construction of 3D capillary network models has become a major focus in the field of tissue engineering, and many such models have been developed for drug testing and toxicity evaluation. The construction of 3D *in vitro* capillary network models is usually influenced by factors such as cell source and type, scaffolds, and mechanical properties [4–6]. Since tissues or organs have a specific range of stiffness, it is necessary to use stiffness adjustable scaffolds to simulate the microenvironment of specific tissues in 3D-model construction [7]. For example, the construction of a highly distributed capillary network formation of endothelial cells (ECs) in a low-stiffness scaffold has been reported [8–10]. On the other hand, good adhesion and proliferation of ECs on the surface of high stiffness scaffolds has also been reported [11,12]. However, a mechanistic description of the differences in behaviors of ECs in the internal and surface of 3D capillary network models has yet to be elucidated.

The development of the brain microvascular system, including a system called the blood-brain barrier (BBB) model, is an important part of capillary network model construction [13]. The BBB is a selective barrier which protects the brain from external aggression, and separates the peripheral and central nervous systems (CNS) [14,15]. It is mainly composed of brain microvascular endothelial cell (BMEC), pericyte (PC),

* Corresponding author. Department of Applied Chemistry, Graduate School of Engineering, Osaka University, Suita, Osaka, Japan.
E-mail address: m-matsus@chem.eng.osaka-u.ac.jp (M. Matsusaki).

https://doi.org/10.1016/j.mtbio.2023.100714
Received 1 May 2023; Received in revised form 9 June 2023; Accepted 23 June 2023
Available online 28 June 2023

and astrocyte (AC) endfeet [15]. BMECs are interconnected by a junctional complex including tight junctions (TJ) and adherens junctions, surrounded by PCs and ACs, and encapsulated in the basal lamina [16]. In the past, many *in vitro* BBB models were developed, such as the transwell model and microfluidic chips [13,17]. Most of them focus on functional studies of the BBB in order to be used for assessing the permeability of drugs [18–20]. However, the mechanical properties of the ECM also influence the behavior of cells in the BBB and the formation of vascular networks, but few report that ECM stiffness affecting BBB model function, and only the effect of substrate on BBB function in 2D culture has been reported [21]. Therefore, it is necessary to construct a 3D BBB *in vitro* model and investigate the relationship between matrix stiffness and BBB formation [22].

We have previously reported a 3D self-organized *in vitro* drop model of the BBB microvasculature which was produced by combining collagen microfibers (CMF) and fibrin gel [23,24]. The interconnected fibers play a crucial role in supporting the migration of BMECs and promoting the formation of capillary-like networks similar to those observed *in vivo*. Furthermore, a modified *in vitro* BBB model based on fibrin gel in a transwell insert was constructed, which also formed a 3D self-assembled microvascular network [25]. The presence of capillary opening holes on the bottom of the scaffold enabled the development of a perfusable microvascular system. This model showed higher high transendothelial electrical resistance (TEER) values relative to the acellular fibrin gels and 2D BMEC monolayers, demonstrating the BBB functional properties of this BBB model. In addition, the BBB model with more hole structure showed a higher transport ability of transferrin receptor (TfR) targeting antibody (AF 647-MEM-189), it is also revealed a higher TfR permeability of anti-TfR antibody (AF 647-MEM-189) than that of control isotype antibody (IgG1), thus demonstrating its potential for use in drug assessment. However, the mechanism of hole structure formation in this model has not been entirely clarified, and we have not identified if the capillary network structure could be regulated by changing the scaffold's mechanical properties.

Herein, we controlled the hole structure of a 3D *in vitro* BBB model by adjusting the elastic modulus of the scaffold to reveal the mechanism of hole formation. The scaffold was constructed by the fibrin gel, which is an important part of the provisional ECM during wound healing. It can be used to observe the mechanical evolution of the ECM during the generation of capillary networks and hole structures because it has a wide range of adjustable mechanical moduli [26–28]. It was found that elastic modulus changes in the scaffold had a notable effect on the behavior of the BMECs, either inside or on the surface of the model. Shallower hole structures and dense internal capillary networks were obtained in the lower-stiffness scaffolds, whereas deeper hole structures were clearly observed in the stiffer scaffolds. In addition, RNA sequencing revealed that genes involved in ECM degradation, tight junction formation, angiogenesis, cell adhesion and migration were up-regulated in stiffer scaffolds. The results suggest the possibility of establishing precisely controlled hole and network structure for BBB models.

2. Materials and methods

2.1. Cell culture

The three cell lines used in this work have been developed and characterized in previous studies: human brain microvascular endothelial cells/conditionally immortalized clone 18 (BMEC) [29], human astrocytes/conditionally immortalized clone 35 (AC) [30], and human brain pericytes/conditionally immortalized clone 37 (PC) [31] were kindly provided by Prof. Furihata from the School of Pharmacy, Tokyo University of Pharmacy and Life Sciences (Hachioji, Tokyo, Japan). Cells were cultured on 225 cm^2 collagen type I coated flasks (Ref. 4160-010, Iwaki, Shizuoka, Japan) or 100 mm diameter collagen type I coated dishes (Ref. 4020-010, Iwaki, Shizuoka, Japan) and incubated at 33 °C, 5% CO_2. All culture media were supplemented with 4 μg/mL Blasticidin S HCl (Ref. R21001, Invitrogen, Waltham, USA) to maintain selective pressure during routine culture. BMECs were cultured in Vasculife (Ref. LEC-LL0005, VEGF-Mv, LifeLine, Frederick, USA) supplemented with 0.5 mL rh FGF-b, 0.5 mL ascorbic acid, 0.5 mL hydrocortisone hemisuccinate, 25 mL L-glutamine, 0.5 mL rh IGF-1, 0.5 mL rh EGF, 0.5 mL rh VEGF, 0.5 mL heparin sulfate, 25 mL fetal bovine serum (FBS) (kit, LifeFactor VEGF-Mv, LifeLine, Frederick, USA), 25 mL supplementary FBS (Gibco ThermoFisher, Waltham, USA), and 1% antibiotic (02892-54, Nacalai Tesque, Kyoto, Japan). AC were cultured in Dulbecco's Modified Eagle Medium (DMEM, Ref. 08458-16, Nacalai Tesque, Kyoto, Japan), complemented with 10% FBS, 1% antibiotic, 5 mL of N_2 supplement x100 (Ref. 17502-048, Gibco ThermoFisher, Waltham, USA). PCs were cultured in Pericyte Medium (Ref. 1201, ScienCell Research Laboratories, Carlsbad, USA), supplemented by 1% Pericyte Growth Supplement 100x, 10% FBS, and 1% antibiotic. ACs and PCs were pre-differentiated at 37 °C for 3 days prior to use for the fabrication of the 3D BBB model.

2.2. Synthesis of FITC-labeled fibrinogen

The synthesis of fluorescein 5-isothiocyanate (isomer I) (FITC)-labeled fibrinogen was prepared as previously reported, with slight modifications [32]. First, 300 mg of fibrinogen (Ref. F8630-5G, Sigma Aldrich, St. Louis, MO, USA) was dissolved in 30 mL 0.1 M bicarbonate buffer (pH = 9, 0.1 M Na_2CO_3: 0.1 M $NaHCO_3$ = 1 : 9) in a flask under stirring at 400 rpm. 30 mg fluorescein 5-isothiocyanate (isomer I) (FITC, Ref. 16151-66, Nacalai, ≥90.0% (HPLC), Kyoto, Japan) was dissolved in 1 mL dimethyl sulfoxide (DMSO, Ref. 043–07216, FUJIFILM Wako, Chemical Pure, Osaka, Japan) in an Eppendorf tube. This FITC solution was then added to the fibrinogen solution under stirring at 400 rpm at room temperature, then left to react in the dark for 1 h at room temperature. The crude product was then transferred into a dialysis film (Mw: 12,000–15,000) and dialyzed in bicarbonate buffer for 3 days during which the buffer was changed 3 times every day. The buffer was changed to MilliQ water on the final day. Finally, the samples were freeze-dried (Freeze Dryer FDU-2200, Eyela, Tokyo, Japan) for 3 days to obtain FITC-fibrinogen sponge and kept in the dark before use.

2.3. Fabrication of 3D BBB models

First, a 10 wt% gelatin solution was prepared using gelatin powder (Ref. G1890, Sigma Aldrich, St. Louis, MO, USA) dissolved in PBS. The gelatin solution was placed in a 37 °C water bath to completely dissolve it. Then, 450 μL of 10 wt% gelatin solution was dispensed on a 24-well plate (Ref. 3820–024, Iwaki, Shizuoka, Japan). The 0.4 μm pore size 24-well culture inserts (Ref. 3470, Costar, NY, USA) were carefully placed on the gelatin solution to ensure that no bubbles were formed below the insert. The 24-well plate was then incubated at 4 °C for 20 min to allow the gelatin solution to gelate. After gelation, the inserts were removed from the gelatin mold and culture insert membranes were peeled off. The membrane-free inserts were put inside a plasma device (Ref. PM100, Yamato Scientific Co., Ltd., Tokyo, Japan) at 40 sccm, 100 W for 1 min plasma treatment to make them hydrophilic. The plasma treated inserts were placed back onto the gelatin mold in the 24-well plate. The BMECs, ACs and PCs were harvested with a Trypsin/EDTA solution composed of 0.25 wt% trypsin (Ref. 209–19182, FUJIFILM Wako, Osaka, Japan) with 0.02 wt% EDTA (Ref. E6758-500G, Sigma Aldrich, St. Louis, MO, USA) and centrifuged at 130 g, 3 min, 25 °C. After centrifugation, the obtained cell pellets were resuspended in the medium and the cell count was measured using a Countess™ 3 Automated Cell Counter (Thermo Fisher, Waltham, USA). For the 3D BBB model, fibrinogen solutions were prepared using DMEM without FBS/antibiotics dissolved at concentrations of 10, 20, 30, 40, and 50 mg/mL (with 1 wt% pre-synthesized FITC-fibrinogen) and 40 μL of each solution was transferred to Eppendorf tubes. Then, 4×10^5 AC, 2×10^5 BMEC, 1×10^5 PC, and 0.2 U thrombin (Ref. T4648-10kU, Sigma Aldrich, St. Louis, MO,

USA) were mixed in 20 μL of DMEM without FBS/antibiotics in another Eppendorf tube. The other BBB models in different conditions were prepared using a similar method, but with three variations of cell number inside the fibrin gel according to demand. Both solutions in the Eppendorf tube were mixed quickly before crosslinking, then the inserts were incubated at room temperature for 20 min to allow the fibrin gel to gelate. The final concentrations of fibrinogen were 7, 13, 20, 27 and 33 mg/mL. The samples were then incubated at 37 °C, 5% CO_2 for 40 min to make the gelatin mold revert to a liquid. After the gelatin melted, 500 μL of warmed PBS was added to the gap between the 24-well plates and the insert to wash away the liquid gelatin remaining on the outer wall of the inserts. The fibrin gels were placed in new 24-well plates with 2.5 mL of triple media comprising Vasculife medium, Pericyte medium, and DMEM/N_2 medium (1:1:1; v:v:v), then incubated at 37 °C, 5% CO_2 overnight. On the next day, the pre-samples were inverted in a 6-well plate (Ref. 3810–006, Iwaki, Shizuoka, Japan) filled with 10 mL of triple media. More BMECs were harvested and 2×10^5 BMEC was resuspended in 60 μL of triple media, then seeded on the top surface of the fibrin gel samples for a second time. The samples were incubated at 37 °C, 5% CO_2 for 6 h to ensure the adhesion of BMECs onto the fibrin gel. After incubation, the inserts were placed on top of 6-well culture plates with a specially designed 24- to 6-well plate adapter. An additional 2 mL of triple media was then added to make a total of 12 mL, and this was then incubated at 37 °C, 5% CO_2. Half of the media was changed (6 mL of the total 12 mL) every 3–4 days during the 7 days or 14 days of incubation.

2.4. Immunofluorescence staining

After 7 days or 14 days of incubation, the 3D BBB models were washed by warmed PBS 3 times then fixed in 4% paraformaldehyde (PFA, Ref. 30525-89-4, FUJIFILM Wako, Osaka, Japan) at room temperature for 1 h. Permeabilization was performed using 0.2% Triton X-100 (Sigma Aldrich, St. Louis, MO, USA) in PBS for 15 min at room temperature. The samples were washed again, then 1% bovine serum albumin (BSA, Ref. A3294-50G, Sigma-Aldrich, St. Louis, MO, USA) in PBS was used for blocking at room temperature for 25 min. The samples were then incubated with primary antibodies: monoclonal mouse anti-human CD31 antibody (Ref. M0823, DAKO, Denmark) diluted at 1/50 in PBS with 0.1% BSA overnight at 4 °C. After washing with PBS 3 times, the secondary antibody: goat anti-mouse secondary antibody (Alexa Fluor 647, Ref. A21235, Thermo Fisher Scientific, Waltham, MA, USA), nuclei stain Hoechst33342 (Ref. H3570, Thermo Fisher Scientific, Waltham, MA, USA), 1/100 dilution in PBS with 0.1% BSA were incubated for 2 h at room temperature in the dark. After washing with PBS 3 times, the samples were observed by confocal laser scanning microscopy (CLSM) (FluoView FV3000, Olympus, Tokyo, Japan) using 30 times magnification.

2.5. Mechanical elastic modulus measurements

All samples were removed from the medium after 7 or 14 days of culture and prepared for compression testing. Compression experiments were conducted to explore the mechanical behaviors under a 1 N loading cell by a 5 mm spherical indenter using an EZ-TEST instrument (Shimadzu, Kyoto, Japan) at a 1 mm/min loading speed. To eliminate any interference during the indentation, only the stable range of 5–10% stress in the stress-strain curve was considered and further fitted into a linear slope. Young's modulus of elasticity was automatically calculated by the instrument's own software.

2.6. Observation with optical coherence tomography (OCT)

An OCT system Cell3iMager Estier (SCREEN Holdings Co., Ltd., Kyoto, Japan) was used to confirm the hole structure of the *in vitro* 3D BBB model. After fixing the *in vivo* 3D BBB model, imaging was performed using OCT with an exposure time of 300 μsec, a scan size of 6000 μm × 6000 μm, a pitch of 7 μm, and a layer pitch of 50 μm. OCT images were processed using ImageJ software. Specifically, the hole structure in each slice of the OCT image was manually selected, then each slice image was masked with the selected hole structure. The masked multiple slices were finally merged (white in Movie S2(c-d)) to obtain a 3D image of the hole structure in BBB mode. The procedures were performed in the following order: freehand selections, Add to ROI manager, Mask, 3D viewer (Fig. S3). Movie S2 shows the process with 14 slices and 34 slices of the masked images for the BBB models at 7 and 33 mg/mL fibrinogen concentration, respectively.

2.7. Calculation of blood capillary length

Blood capillaries from the fluorescence images were extracted and skeletonized by ImageJ software (Fiji, Ver. 1.53) [33], then their average length was analyzed and calculated by ImageJ. The procedures were performed in the following order: Gaussian Blur, Skeletonize (2D/3D), Analyze Skeleton (2D/3D).

2.8. RNA extraction from models

RNA extraction was performed on three types of 3D BBB models (n = 2): ACs and PCs inside the fibrin gel with BMECs seeded on the bottom surface at 33 mg/mL fibrinogen ("Hol" group); ACs, PCs, BMECs inside the fibrin gel without BMECs on the bottom surface at 7 mg/mL fibrinogen ("Net" group); No cells inside the fibrin gel and BMECs seeded on the bottom surface at 33 mg/mL fibrinogen as a control group ("BM" group). Samples were first washed once in PBS and then transferred to 600 μL of Lysis Buffer (PureLink® RNA Mini Kit, Ref. 12183020, Thermo Fisher Scientific MA, USA) prepared with 1% of 2-mercaptoethanol, then the tissue was pipetted until fully dissolved. The homogenate was transferred to a sterile Eppendorf tube and centrifuged at 12,000 g for 2 fmin, then the supernatant was used for RNA extraction, following the PureLink® RNA Mini Kit protocol (Thermo Fisher Scientific, MA, USA). Extracted RNA was quantified using a NanodropTM N1000 device (Thermo Fisher Scientific, MA, USA).

2.9. RNA sequencing and data analysis

The above samples after RNA extraction were sent to the Genome Information Research Center (Osaka University, Japan) for RNA sequencing. Full-length cDNA was generated using a SMART-Seq HT Kit (Clontech, TaKaRa, Shiga, Japan) according to the manufacturer's instructions. An Illumina library was prepared using a NexteraXT DNA Library Preparation Kit (Illumina, California, USA) according to SMARTer kit instructions. Sequencing was performed on an Illumina NovaSeq 6000 sequencer (Illumina, California, USA) in the 100-base single read mode. Sequenced reads were mapped to the human reference genome sequences (hg19) using TopHat version 2.1.1. The fragments per kilobase of exons per million mapped fragments (FPKM) were calculated using Cuffnorm version 2.2.1. The raw data have been deposited in the NCBI's Gene Expression Omnibus database. The iDEP (http://bioinformatics.sdstate.edu/idep/) differential expression analyses and global analysis of the RNA-sequencing expression data were performed using BioJupies (https://amp.pharm.mssm.edu/biojupies/) [34]. Gene Ontology (Fig. 6(a–c); Fig. S6, Supporting Information) and Pathway Enrichment (Fig. S7, Supporting Information, using the WikiPathways_2021 library) and analysis results were generated by analyzing the up-regulated and down-regulated gene sets using Enrichr (Kuleshov et al., 2016). The up-regulated and down-regulated gene sets were generated by extracting the 500 genes with the respectively highest and lowest values of T-score from the gene expression signature, then submitted to Enrichr and plotted [35,36]. For the Volcano Plot (Fig. S8, Supporting Information), gene fold changes were transformed using log2 and plotted on the x-axis. p-values were corrected using the Benjamini–Hochberg method,

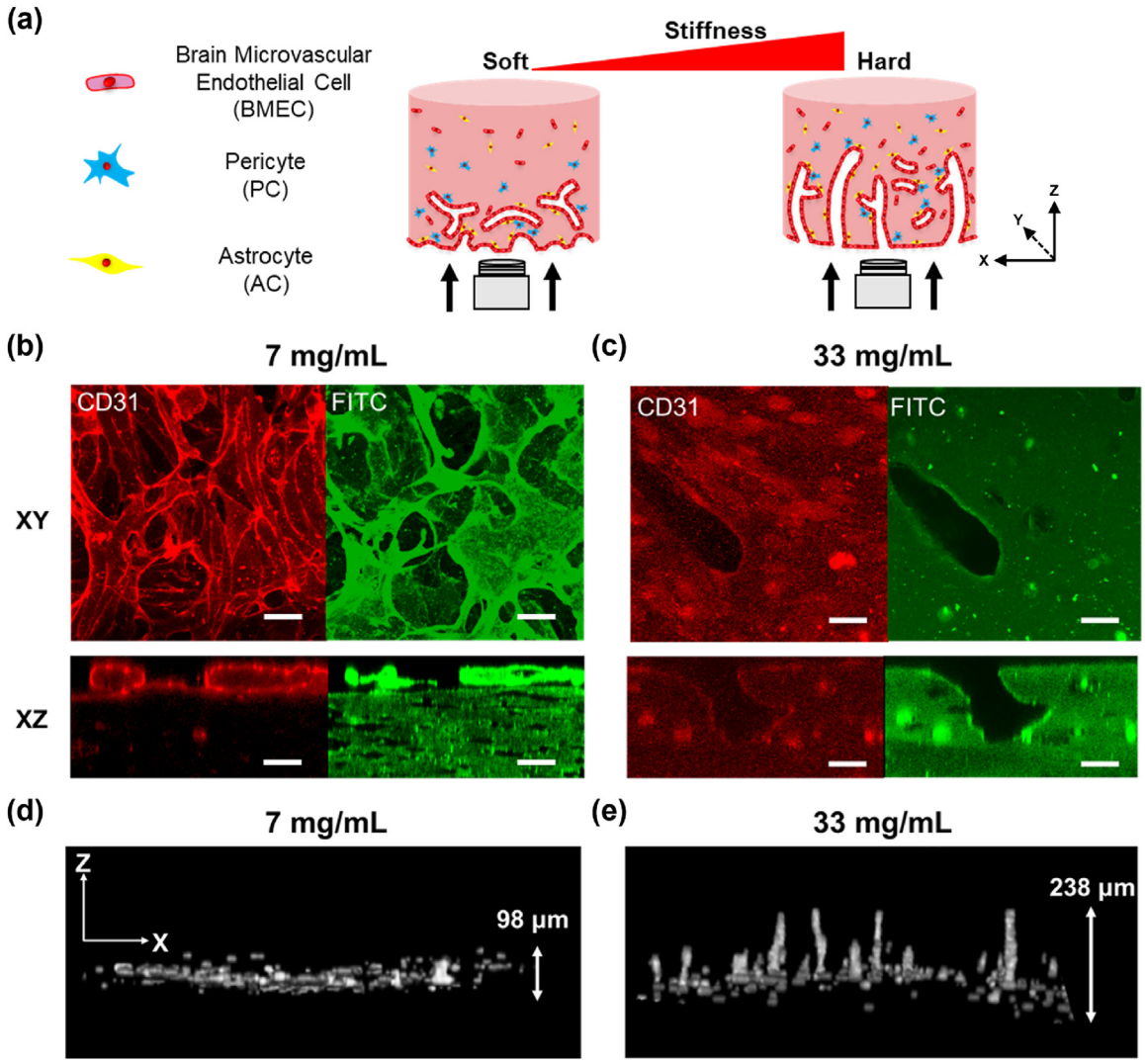

Scheme 1. (a) Schematic illustration of network and hole formation depending on the stiffness of scaffolds, and CLSM observation position in the 3D BBB models. (b–c) CLSM images of CD31 immunostaining and FITC-fibrin gel in 3D BBB models at different fibrinogen concentrations of 7 and 33 mg/mL, after 14 days of incubation. Scale bar: 30 μm. (d–e) 3D reconstruction images of the hole structures in the 3D BBB models obtained by OCT at 7 (left) and 33 (right) mg/mL fibrinogen concentration, after 14 days of incubation. The Z axis was enlarged 5 times by ImageJ.

transformed using −log10, and plotted on the y-axis.

2.10. Statistical analysis

All data are expressed as means ± SD. The values represent the means ± SD from three independent experiments, unless otherwise stated. Statistical comparisons between groups were analyzed using two-tailed Student's t-tests. A value < 0.05 was considered statistically significant. These are indicated in the graphs as $*p < 0.05$, $**p < 0.01$. N.D. denotes not detected. N.S. denotes no significant difference.

3. Results

3.1. Influence of the fibrin gel stiffness on the BMEC capillary network and hole formation

First, we fabricated a 3D BBB model using BMECs, ACs and PCs seeded in inside the fibrin gel and BMECs seeded on the bottom surface of the fibrin gel with varying stiffnesses to investigate the BMECs behavior in this model. Different stiffnesses could indeed be achieved by varying the fibrinogen concentration [37], from 7 mg/mL (soft) to 33 mg/mL (hard). As shown in Scheme 1(a), structural changes were observed in the holes and a capillary network was formed by BMECs in the fibrin gels with different stiffnesses. After immunostaining, all 3D BBB models were observed with confocal laser scanning microscopy (CLSM) at different depths in the fibrin gel. In this 3D BBB model, BMECs on the bottom surface can form a monolayer and migrate over time to form hole structures, while the BMECs seeded inside the fibrin gel can form a capillary network. We also performed compression testing on all samples to verify and analyze the effect of fibrinogen concentration on the model elastic modulus. For this construction, we first discovered that 3D BBB models with hole structures of different depths could be generated by controlling the elastic modulus.

Scheme 1(b-c) and Fig. S1 show fluorescence images obtained by CLSM. The samples were immunostained for CD31 in the FITC-labeled fibrin gel. CD31 is a typical marker of endothelial cells commonly used for observing the capillary network structure formation. The FITC-fibrinogen's photochemical stability allows it to maintain a high intensity over long periods of fluorescence exposure, which was preferable for hole structure observation and analysis. Scheme 1(b-c) and Fig. S1(d) show samples after 14 days of incubation, where we found some sub-circular structures on the surface with extensions to the interior of the gel,

named hole structures. The CD31-stained and FITC images clearly show the hole structure (XY planes) and side view (XZ planes) of the models. Fig. S2 shows the internal structure in the 3D BBB models with different stiffnesses after 7 and 14 days culture. Overall, hole structures were confirmed on all the 3D BBB models' surfaces in different fibrinogen concentrations, but all had different characteristics. At a low concentration of fibrinogen, it can be seen that many holes were formed and their extension to the interior (Z-direction) is shallow. In addition, the BMECs inside the model were well grown and connected to form a capillary network as shown in Fig. S2(d). At higher fibrinogen concentrations (especially at 33 mg/mL), there were fewer holes formed on the surface of the model, but deep holes were formed that were internally connected to the outside environment. In contrast to the model with low fibrinogen concentration, the BMECs inside this model did not form a capillary network but existed as single cells (Fig. S2(f)). Figs. S1(a–c) and Figs. S2(a–c) show samples after 7 days of incubation. Similarly, after 7 days of incubation, deep holes were not formed on the surface of the models with a low elastic modulus, demonstrating that this phenomenon is not caused by the length of culture time. In this group of samples, the hole and capillary network formation pattern changed little in comparison with the 14-day incubated model. Scheme 1(d-e) shows 3D BBB models observed by optical coherence tomography (OCT) and processed by ImageJ. The 3D images of hole structures were obtained by merging multiple slices and the specific processing method is shown in Fig. S3. The range of the images is after calculation and shows the Z-direction depth in the 3D BBB models with 7 and 33 mg/mL fibrinogen concentrations is 98 μm and 234 μm, respectively. It also demonstrates the difference of hole depth in the soft and hard 3D BBB models.

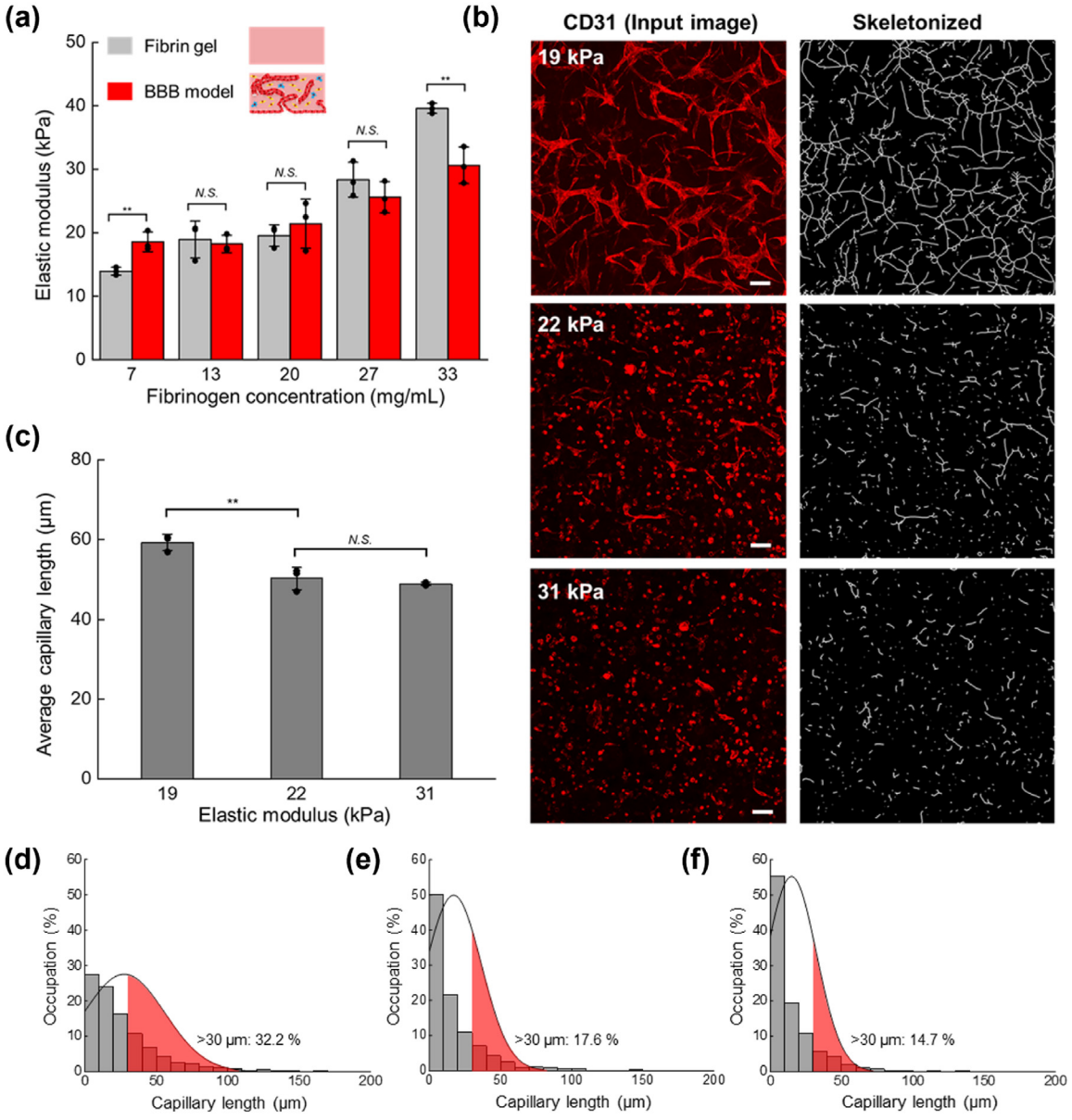

Fig. 1. (a) Elastic modulus of 3D BBB models after 7 days of incubation by compression testing. (b) CLSM image for blood capillary network structure in the 3D BBB models at 19–31 kPa after CD31 immunostaining and the skeletonized images processed by ImageJ software. Scale bar: 100 μm. (c) Calculated blood capillary length of 3D BBB models at 19–31 kPa by ImageJ software (n = 3). Data are presented as means ± S.D. (d–f) The ratio and normal distribution of capillary length of 3D BBB models at 19 (d), 22 (e), 31 (f) kPa.

3.2. Influence of elastic modulus on the capillary network inside the 3D BBB models

To further characterize the relationship between fibrinogen concentration and elastic modulus in fibrin gels, the elastic modulus of acellular fibrin gels and 3D BBB models at different fibrinogen concentrations (7, 13, 20, 27, and 33 mg/mL) was measured by compression testing, as shown in Fig. 1(a). In both the acellular fibrin gel and BBB models groups, the elastic modulus increased with an increase in fibrinogen concentration, due to the raised crosslinking degree in the fibrin gel. In samples with 7 mg/mL fibrinogen concentration, the 3D BBB models had a higher elastic modulus than acellular fibrin gel, but at a high fibrinogen concentration of 33 mg/mL, the acellular fibrin gel had a higher elastic modulus than the 3D BBB models. We hypothesized that the formation of a capillary network influences the connection structure inside the models and has an impact on the elastic modulus changes so we evaluated the capillary network in the 3D BBB models. Fig. 1(b) shows capillary network confocal fluorescence images at 7 days culture in the 3D BBB models with an elastic modulus of 19, 22 and 31 kPa (7, 20 and 33 mg/mL). At a low elastic modulus (19 kPa), the BMECs formed a connected capillary network. However, at a high elastic modulus (22 and 31 kPa), most of the BMECs existed as single cells, while only a few formed short capillaries. To quantify the capillary length, ImageJ software was used to extract the skeletal outline of the capillary network at each concentration. The average length of the extracted skeleton was calculated as shown in Fig. 1(c). From Fig. 1(b), we can quantify the size of a CD31 positive spot (BMEC aggregation) at around 15 μm, so statistics larger than 2 spots (30 μm) were counted. From the calculated data, the average capillary lengths of the models were 59.3 μm, 50.2 μm and 48.9 μm for the 3D BBB models with a respective elastic modulus of 19, 22, and 31 kPa (Fig. 1(c)). These data cannot fully describe the relationship between concentration and capillary length, so the percentage of interval length of capillaries and a normal distribution plot were calculated. As shown in Fig. 1(d-f), 32.2% of the capillaries were longer than 30 μm in the models with an elastic modulus of 19 kPa, but only 14.7% in those of 31 kPa models. These results demonstrate that capillary formation becomes difficult inside 3D BBB models under conditions of increasing elastic modulus, which is consistent with previous works [8,9,38], indicating that the internal structure of the model can be regulated by adjusting the scaffold stiffness.

3.3. Influence of elastic modulus and culture time on the hole structure formation

We next performed quantitative analysis of the hole structure to gain further insights into the effect of differences in elastic modulus and culture time. Quantitative analysis of the hole structures' number, diameter, and depth was based on FITC fluorescence images, as CD31 staining is susceptible to attenuation from prolonged irradiation and produces weaker signals in deeper regions of the 3D BBB model, while FITC-fibrinogen has a stronger signal and responds to the physical morphology of the hole structure. Therefore, to demonstrate the overlap of CD31 and FITC signals, colocalization analysis of CD31 and FITC images was required. Fig. 2(a) shows the method of colocalization analysis using Imaris software. A hole structure was first selected, FITC and CD31 in the same area were quantified separately using Imaris to obtain two specific values of fluorescence intensity, and then the percentage of colocalization was calculated by dividing the average fluorescence intensity value of CD31 with the average fluorescence intensity value of FITC. As shown in Fig. 2(b), 10 different holes were selected at different

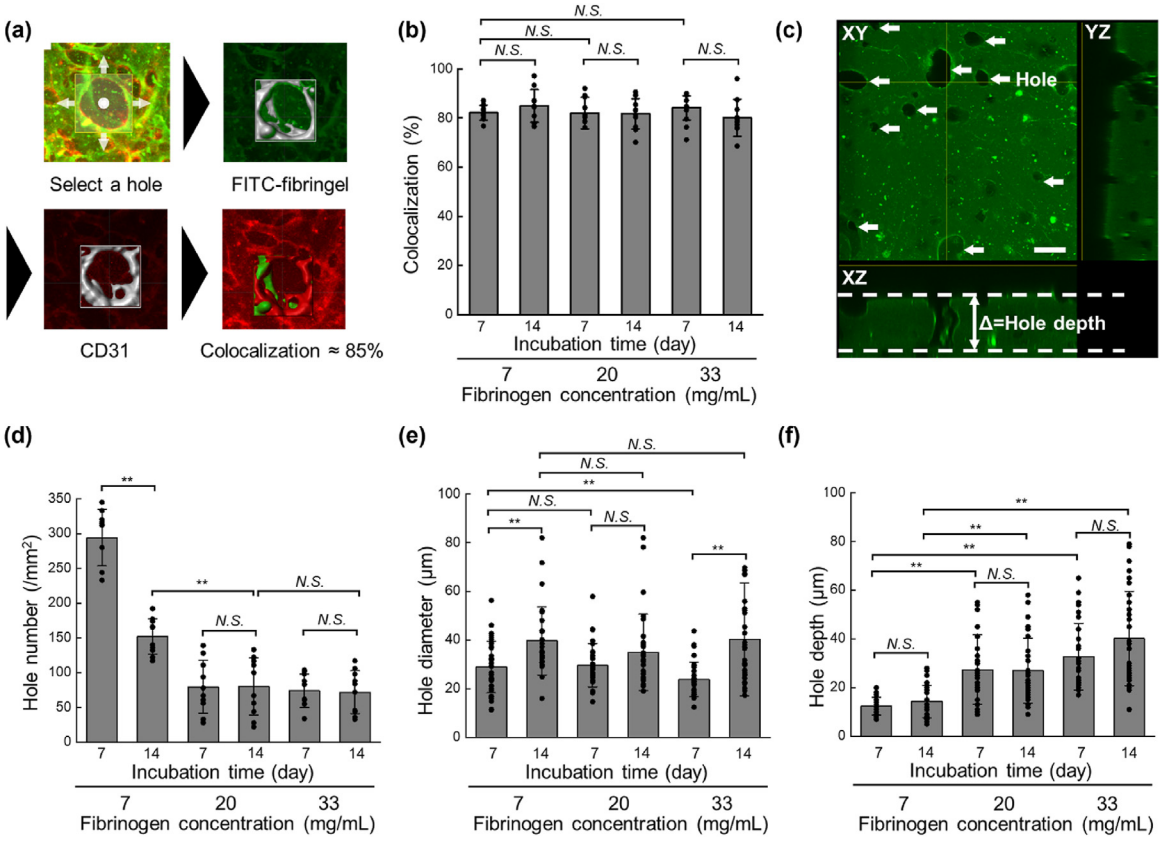

Fig. 2. (a) Hole structure colocalization between CD31 and FITC-fibrin gel images, colocalization was calculated by Imaris. (b) The calculated colocalization at 7–33 mg/mL fibrinogen concentration after 7 and 14 days of incubation (n = 10). N.S. means no significant differences. (c) Representative CLSM image of FITC-fibrin gel to describe hole position (arrow) and depth (double arrow). Scale bar: 50 μm. Calculated hole (d) number, (e) diameter, (f) depth of the 3D BBB models at 7–33 mg/mL fibrinogen concentration after 7 and 14 days of incubation (n = 10 for number, n = 30 for diameter and depth, respectively). Data are presented as means ± S.D.

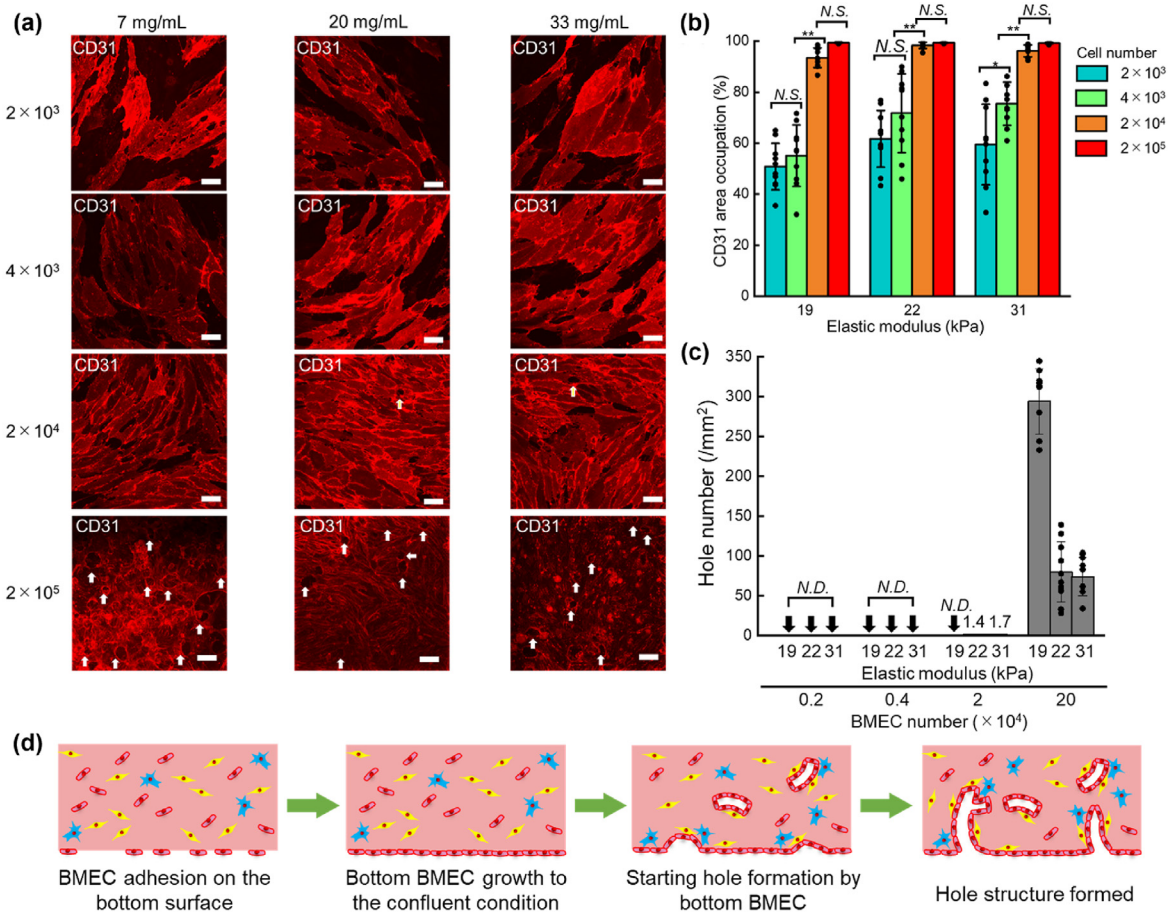

Fig. 3. (a) CD31 immunostaining images of the 3D BBB models at 7–33 mg/mL fibrinogen concentration by varying seeding BMEC density to the bottom surfaces after 7 days of incubation. Scale bar: 50 μm. (b) CD31 area occupation of 3D BBB models with 19~31 kPa elastic modulus with different BMEC seeding density at 0.2, 0.4, 2 and 20 × 10^4, respectively (n = 10). (c) Calculated hole numbers of 3D BBB models with 19~31 kPa elastic modulus by varying BMEC seeding density at 0.2, 0.4, 2 and 20 × 10^4, respectively (n = 10). Data are presented as means ± S.D. (d) Schematic illustration of growth and hole structure formation processes of the bottom BMECs.

locations on each sample to ensure accuracy and reproducibility. The results showed a colocalization percentage of FITC and CD31 of more than 80% on all samples. The FITC fluorescence images can therefore be used for the characterization of the holes. Fig. 2(c) and Fig. S4 show the location of the hole (white arrow), the XZ planes image shows the hole clearly and the hole depth can be calculated by measuring the difference between the lowest and highest positions (double arrow). From the calculation results, the number of holes was greatest in the low elastic modulus condition (290 holes/mm^2). Although there were fewer holes for models after 14 days of culture (150 holes/mm^2), they were still about two times higher than the numbers for the 20 mg/mL and 33 mg/mL fibrinogen models. For the 20 mg/mL and 33 mg/mL fibrinogen models, there were no significant changes in the number of holes for models after 7 or 14 days of culture (Fig. 2(d)). The size of the hole was also calculated (Fig. 2(e)). It was found that the hole diameter of most models was not significantly different in the same culture time, around 25–40 μm, and only the 33 mg/mL model after 7 days culture was found to have smaller holes than the 7 and 20 mg/mL models. For models with the same fibrinogen concentration, the diameter of the holes showed a trend of increasing with increasing culture time. For the models at 7 mg/mL fibrinogen concentration, in relation to the results of hole number, it was demonstrated that a longer culture time led to an increase in hole size and finally the number of holes decreased. With the increase of fibrinogen concentration, the average depth of the holes increased, reaching around 80 μm in the 33 mg/mL models (Fig. 2(f)). At the same fibrinogen concentration, the average depth of the holes in all samples was not significantly changed by culture time. However, according to the figure, the average hole depth showed a trend of becoming slightly deeper with increasing culture time.

The quantitative analysis is in accordance with the qualitative observation obtained from the CLSM images in Scheme 1. It shows various properties of holes in the 3D BBB models, such as size and number, can be adjusted by varying the scaffold elastic modulus, which has important implications for the fabrication of a controllable 3D BBB model.

3.4. *Effect of elastic modulus and BMEC seeding density on the hole formation*

For the 3D BBB model in this study, the proliferation and migration of BMECs on the bottom surface contribute to the hole formation, but the exact mechanism of this formation remains unclear. Therefore, we investigated if the BMEC seeding density on the bottom surface of the hydrogel would impact the hole formation. The seeding densities of BMECs on the bottom surface in 3D BBB models were thus changed to 2 × 10^3, 4 × 10^3, and 2 × 10^4, which was 100, 50, and 10 times lower than the 2 × 10^5 BMECs on the original 3D BBB models' surface. After 7 days of incubation, models were immunostained by CD31 and the fluorescence images were also obtained by CLSM as shown in Fig. 3(a). The elastic modulus values for the 3D BBB models with different fibrinogen concentrations were 19 (7 mg/mL), 22 (20 mg/mL), and 31 kPa (33 mg/mL) obtained from Fig. 1(a). Independently of elastic modulus, were not

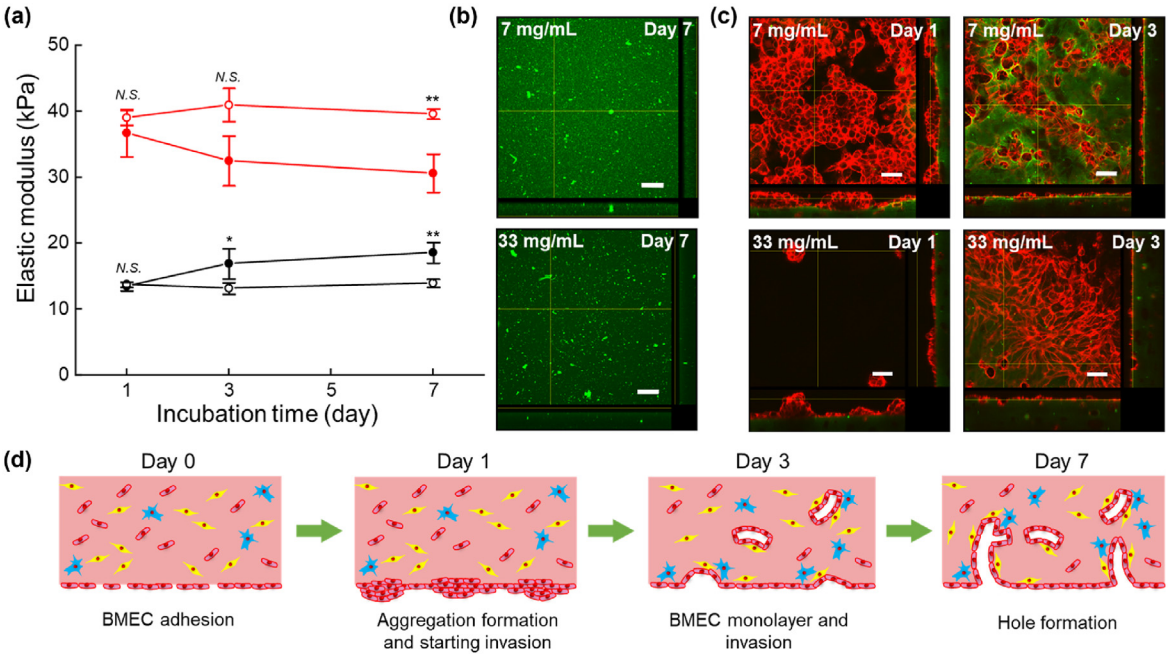

Fig. 4. (a) Elastic modulus of 3D BBB models after 1–7 days incubation by compression testing. The fibrinogen concentration is 7 (black) and 33 mg/mL (red), the model is an acellular fibrin gel (○) and a 3D BBB model (●), respectively (n = 3). Data are presented as means ± S.D. (b) CLSM images of acellular FITC-fibrin gel at 7–33 mg/mL fibrinogen concentration after 7 days of incubation. Scale bar: 50 μm (c) CLSM images of 3D BBB models at 7–33 mg/mL fibrinogen concentration after 1 or 3 days of incubation, the Z range is 20 μm for all conditions. Scale bar: 50 μm. (d) Schematic illustration of bottom BMEC behavior over the time leading to the hole formation. (For interpretation of the references to colour in this figure legend, the reader is referred to the Web version of this article.)

formed in the models with 0.2×10^4 and 0.4×10^4 BMECs, due to the insufficient BMECs coverage on the bottom surface. Even for the 2×10^4 models, only a few holes were found in the high concentration condition. Quantitative analysis of CD31 area occupation was calculated by ImageJ software and the hole number was counted (Fig. 3(b and c)). Even in 3D BBB models with different elastic moduli, as the BMEC seeding density increased, the coverage of BMECs gradually increased from 50% to around 70% in the models with 0.2×10^4 and 0.4×10^4 up to around 95% in the 2×10^4 model, but the hole structures density was only 1.4 and 1.7/mm^2, which was much lower than the original 3D BBB model. This shows that BMECs did not migrate to the inside of the model at a lower BMEC seeding density.

From these results, we described the potential mechanism of BMEC behavior during the formation process of hole structures at a low BMEC seeding density condition as shown in Fig. 3(d). After BMECs are seeded and adhere to the bottom surface of the 3D BBB model, they gradually grow to form a confluent monolayer. After the BMECs on the surface reach a certain number, they may start to migrate inside the fibrin gel, and eventually these migration behaviors may make the hole appear on the surface of the 3D BBB models.

3.5. Time lapse of hole formation in the 3D BBB model

To investigate the changes in the 3D BBB model during culture which lead to the formation of the hole structure, the elastic modulus and CD31 immunostaining was performed on the 3D BBB model was evaluated after 1 and 3 days of incubation. Fig. 4(a) shows the time-dependent changes of elastic modulus of the acellular fibrin gel and 3D BBB model with a fibrinogen concentration of 7 and 33 mg/mL. In the acellular fibrin gel group, we found almost no change in the elastic modulus after different culture times irrespective of fibrinogen concentration. On the other hand, in the 3D BBB model groups, the elastic modulus of the 33 mg/mL fibrinogen models decreased with increasing culture time (37 kPa to 31 kPa), whereas 7 mg/mL fibrinogen models showed increased elastic modulus with increasing culture time (13 kPa to 19 kPa). Fig. 4(b) shows CLSM images for acellular FITC-fibrin gel after 7 days of culture at 7 and 33 mg/mL fibrinogen concentration. The surface of the incubated fibrin gel was smooth, with no hole structure, which excluded the possibility that hole structure formation was due to the self-degradation of fibrin gel in a 3D BBB model. Fig. 4(c) shows projection images of the 3D BBB model with a Z range of 20 μm for all conditions, starting from the bottom to the inside of the models. Overall, BMECs had aggregated on the surface of the 3D BBB models at day 1, while also starting to invade the interior of the gel. At day 3, the BMECs on the surface congregated, forming a monolayer, and a few hole structures also appeared, as also shown in Movie S1. Furthermore, for the 3D BBB models with different elastic moduli, we observed similar BMECs morphology on day 1. However, on day 3, more hole structures had started to form on the surface of softer (7 mg/mL) 3D BBB models, the BMECs had formed a confluent layer and a few hole structures had started to form on the surface of harder (33 mg/mL) 3D BBB models. This suggests that at the early period of hole structure formation, BMECs already generate expression differences on the surface of the 3D BBB model with different elastic moduli. From these results, the potential mechanism of the time-dependent structural changes leading to the formation of hole structure is summarized in Fig. 4(d). After the BMECs adhered to the bottom of the model, they proliferated, formed cell aggregates, and started to migrate inside the model. Subsequently, the BMEC monolayer and holes formed with continued incubation.

3.6. Incorporation of supporting cells on the hole structure formation of scaffolds with different stiffnesses

We next evaluated the effects of ACs and PCs on hole structure formation in the different elastic modulus 3D BBB models. Although the BBB model configuration differed from the original BBB model, it was estimated that the increased fibrinogen concentration would have a similar impact on the stiffness of the fibrin gel, as seen in Fig. 1(a). Varying the fibrinogen concentration from 7 to 33 mg/mL would thus lead to the formation of a soft and hard gel, respectively. As seen in Fig. 5(a-d), a

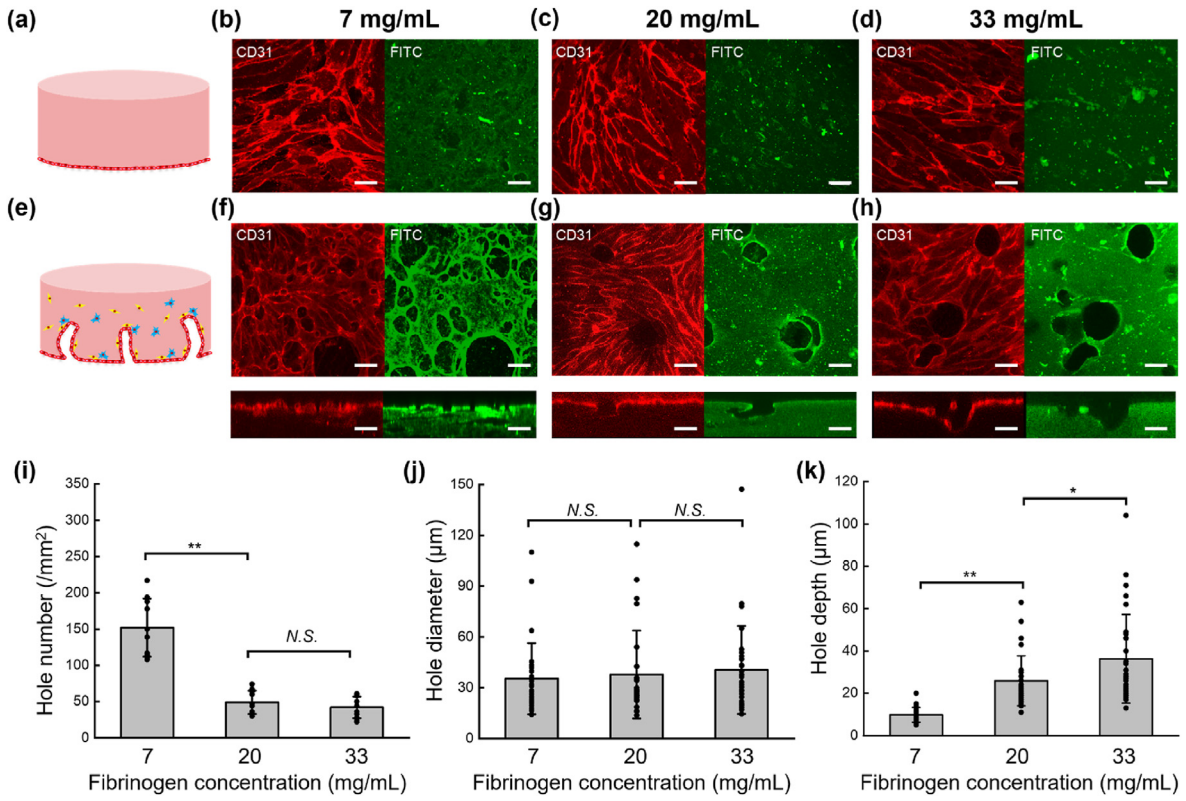

Fig. 5. (a) Schematic illustration of the model without cells inside the fibrin gel and only BMECs on the bottom surface. (b–d) CLSM images of CD31 immunostaining and FITC-fibrin gel in samples without cells inside the fibrin gel with a bottom BMEC monolayer at different fibrinogen concentrations of 7~33 mg/mL, after 7 days of incubation. Scale bar: 30 μm. (e) Schematic illustration of the model without BMECs inside the fibrin gel. (f–h) CLSM images of CD31 immunostaining and FITC-fibrin gel in samples without AC and PC cells inside the fibrin gel with a bottom BMEC monolayer at different fibrinogen concentrations of 7~33 mg/mL, after 7 days of incubation. Scale bar: 30 μm. Calculated hole (i) number, (j) diameter, (k) depth of samples without AC and PC cells inside the fibrin gel and with a bottom BMEC monolayer at 7–33 mg/mL fibrinogen concentration after 7 days of incubation (n = 10 for number, n = 30 for diameter and depth, respectively). Data are presented as means ± S.D.

modified model was prepared by removing cells inside the fibrin gel and with only BMECs seeded on the bottom surface, named the "BM" model. After 7 days of incubation, no hole structures were detected on any of the 3 types of BM models, independently of the fibrinogen concentrations used. The models of ACs and PCs (w/o BMECs) inside the fibrin gel with surface BMECs were also evaluated, as shown in Fig. 5(e–h). A hole structure was found at all concentrations of models, demonstrating that ACs and PCs have an important role in promoting the formation of a hole structure. This could be due to the secreted factors by ACs and PCs, such as vascular endothelial growth factor (VEGF), basic fibroblast growth factor (bFGF), and angiopoietin 1 (ANG-1) [39]. The hole number of w/o BMEC models were 152 (7 mg/mL), 49 (20 mg/mL), and 42 holes/mm^2 (33 mg/mL), showing that the model with the low fibrinogen concentration yielded the highest value (Fig. 5(i)). For calculated hole diameter, there were no significant differences between any of the models (Fig. 5(j)). The calculated hole depths were 10, 26, and 36 μm for the 7, 20 and 33 mg/mL fibrinogen concentrations, respectively (Fig. 5(k)). These values are within the same range as the original 3D BBB models. The phenomenon of more and shallower hole structures for the soft model (7 mg/mL) and fewer and deeper hole structures for the hard model (33 mg/mL), is in accordance with the observations from Fig. 2.

3.7. Gene expression analysis

RNA sequencing was performed to investigate the effect of hole structure formation on gene expression. Three types of models were designed, the hole structure model (Hol), the capillary network model (Net) and only BMECs on the model bottom surface (BM), as shown in Fig. 6(a–c). All the models were incubated for 7 days and then total RNA was collected and sequenced for comparison. First, principal component analysis (PCA) was performed for all genes to evaluate the similarity between the samples (Fig. S5). Significant differences were observed between the hole structure (Hol), network structure (Net) and only BMEC on bottom surface (BM) models, while the differences between Hol and Net were relatively small. To evaluate the functional effects of these gene expression changes, we performed GO enrichment analysis of the up and down-regulated genes. The up-regulated terms of Hol vs Net, Hol vs BM, and Net vs BM are shown as in Fig. 6(d–f). These terms are GO biological process, molecular function, and cellular component, respectively, and the results are sorted in order of decreasing p-value. From these differences, it seems that the enrichment terms related to protein cleavage, extracellular matrix, cytokines, and lysosomes are important in Hol. For BM, both Hol and Net show enrichment terms associated with proliferation (mitosis). The above results show that Hol and Net have extremely similar gene expression due to the same cell types, initial BMEC, AC, and PC seeding numbers and culture times used in these models. Therefore, in the analysis of key genes in cell adhesion, cell migration, focal adhesion, tight junction formation, angiogenesis, and ECM degradation, we considered genes with fold changes that had a relatively large value to be differentially expressed genes. The heat map of the selected key genes in each sample is shown in Fig. 6(g), showing differential properties of these genes in Hol, Net, and BM. Compared to Net, 12 genes were up-regulated in Hol and these genes may be associated with the formation of holes. Therefore, the specific fold changes of the differential genes were counted and are summarized in Fig. 6(h and i). From the results, MMP1, MMP10, ACE genes coding for ECM and protein degradation; CLDN5 coding for the tight junction protein Claudin-5; ITGA1, CD36 coding for proteins involved in cell adhesion; ANGPT1, ANGPTL1, COL21A1 coding

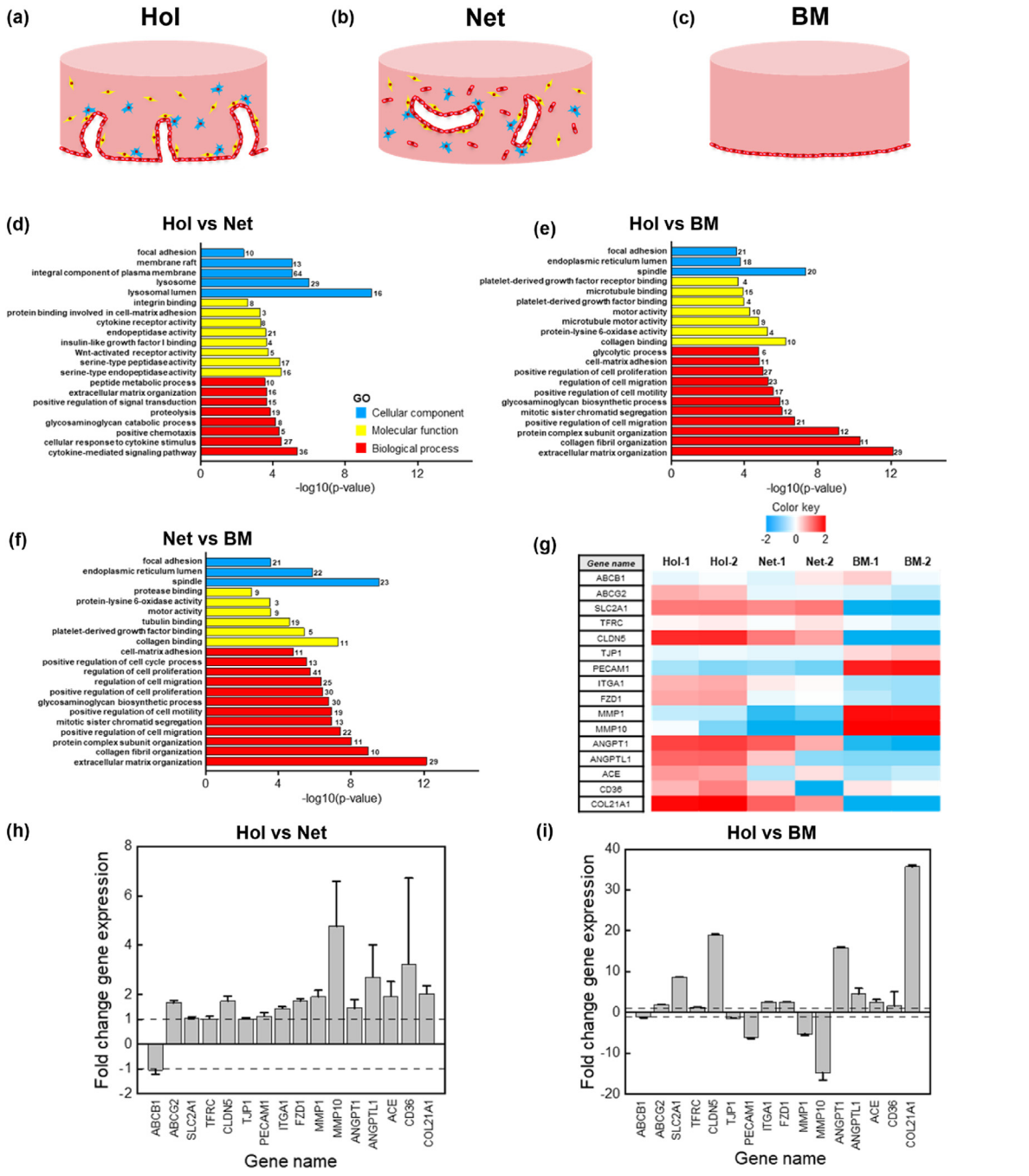

ABCB1 (ATP binding cassette subfamily B member 1): Permeability glycoprotein, transporter
ABCG2 (ATP binding cassette subfamily G member 2): BCRP, transporter
SLC2A1 (solute carrier family 2 member 1): GLUT1, transporter
TFRC (Transferrin receptor 1): TfR, transporter
CLDN5 (Claudin-5): Tight junction protein
TJP1 (Tight Junction Protein 1): ZO-1, tight junction
PECAM1 (Platelet And Endothelial Cell Adhesion Molecule 1): CD31, endothelial marker
ITGA1 (Integrin alpha-1): Collagen receptor, related to cell adhesion and migration
FZD1 (Frizzled class receptor 1): Focal adhesion, Wnt signaling protein receptor
MMP1 (Matrix Metallopeptidase 1): ECM degradation
MMP10 (Matrix Metallopeptidase 1): ECM degradation
ANGPT1 (Angiopoietin 1): Regulation of angiogenesis, endothelial cell survival, proliferation, migration, adhesion
ANGPTL1 (Angiopoietin Like 1): Vascular endothelial growth factor
ACE (Angiotensin I converting enzyme): CD143, Proteolysis
CD36 (Cluster of differentiation 36): cell adhesion molecule
COL21A1 (Collagen Type XXI Alpha 1 Chain) : Vascular formation, collagen

Fig. 6. RNA sequencing comparison of 3 types of models (n = 2); (a) ACs and PCs inside the fibrin gel with BMECs on the bottom surface at 33 mg/mL fibrinogen, a hole structure formed on the model surface but without a capillary network inside. (b) ACs, PCs, BMECs inside the fibrin gel without cells on the bottom surface at 7 mg/mL fibrinogen, a capillary network formed inside the model but without a hole structure on the model bottom surface. (c) Without cells inside the fibrin gel and only BMECs on the bottom surface at 33 mg/mL fibrinogen as a control group, neither hole nor capillary networks could be formed. (d–f) The gene ontology (GO) of biology process, molecular function, cellular component terms for up-regulated genes in Hol vs. Net (control) group, Hol vs. BM (control) group, Net vs. BM (control) group, respectively. The number on each term bar is the number of genes contained. (g) Heatmap shows the different gene expression pattern of BBB transporter, tight junction formation, cell adhesion, cell migration and angiogenesis. (h–i) The different expression of genes in Hol respectively compared to Net and BM, were represented by the calculation of gene fold change (n = 2). Genes with fold change values greater than 1 are up-regulated, those with fold change values less than −1 are down-regulated. Data are presented as means ± S.D.

for proteins involved in angiogenesis processes; FZD1 coding for focal adhesion, were up-regulated in Hol compared to Net.

4. Discussion

Herein, based on a reported method in our laboratory [24], we attempted to build an *in vitro* model of a BBB, which has a hole structure on the model surface to effectively connect the model inside the microenvironment with the outside environment for transportation. The hole structure is similar to the lumen structure in the process of vascular sprouting. Specifically, new vascular sprouting is guided by endothelial tip cells and forms a lumen structure after proliferation and migration of endothelial stalk cells [40]. The formation of lumen structure is often found in the interior of models such as 3D microfluidic chips [41]. However, we found for the first time that the formation of lumen structure on the tissue surface and its characteristics were regulated by varying the matrix stiffness. Hydrogels are known to provide a convenient and structurally stable 3D microenvironment for cultured cells [42,43]. In general, even small changes in the 3D microenvironment, such as scaffold stiffness, can influence the behavioral expression of cells [44,45]. Therefore, regulating the stiffness of a hydrogel in the *in vitro* BBB mode is beneficial for simulating organs such as the brain [13,46]. At first, 3D BBB models were fabricated at different fibrinogen concentrations since increased fibrinogen concentration can increase the elastic modulus of fibrin gel [47]. In subsequent compression testing, we also demonstrated that there was a positive relationship between fibrinogen concentration and elastic modulus. As expected, the obtained 3D BBB models with different fibrinogen concentrations had large phenotypic differences, but surprisingly these differed from previous reports in the literature. We originally thought the BMECs on a soft gel would more easily form a deeper hole structure as previous reports have shown that soft gel is more conducive to the migration of endothelial cells inside the model [48,49], and the migration of BMECs into the model is the reason for hole formation. However, in our study, a shallow hole structure was generated on the softer 3D BBB model, and a deep hole structure was generated on the harder 3D BBB model. We have not found any similar cases in past reports. The size of the hole structure seemed to be random and was not changed significantly according to the 3D BBB model culture time and elastic modulus. We believe it is highly probable that BMECs show different gene expression on scaffolds of differing stiffness.

The formation of a capillary network within different 3D BBB models was also quantitatively analyzed. It is noteworthy that although the average capillary length at a low concentration was only about 15% higher than at a high concentration, the interval statistics showed that not only were more capillaries generated at a low concentration but also the ratio of long capillaries was much higher than in the high concentration model. Past reports have shown that increasing fibrinogen concentration results in higher fibril density and smaller pore size of the gel network, which makes it more difficult for BMECs to migrate and remodel the ECM in fibrin gels [27]. In addition, the transmission of factors that regulate cell adhesion and migration, such as the integrin, are also barriered by the fibrin gel networks [50]. Therefore, capillary formation is co-regulated by matrix elastic modulus, gel network size, and integrin transmission. Compression testing showed that the elastic modulus of the 3D BBB model was greater than the fibrin gel at a low concentration, but this was reversed at a high concentration. Combined with the results of hole structure and capillary network evaluation, we can speculate that for the low concentration model, a well-connected and dense capillary network will serve to enhance the model strength, and the capillaries can be considered as fibers. From a mechanical point of view, long fibers in the material will improve its mechanical properties [51]. Although many hole structures are generated on the model surface, they have only a small impact on the model construction due to their shallow depth. Therefore, the 3D BBB model under low concentration conditions possesses a higher elastic modulus. On the other hand, in the high elastic modulus model, deeper hole structures may lead to model instability and collapse, while inside the model, the individual BMECs or short capillaries cannot enhance the model strength [52]. Therefore, the modulus of the 3D BBB model at high concentrations is lower than normal fibrin gel.

Next, the holes were evaluated with a low number of BMECs seeded on the model surface, which contributed to our explanation for the process of hole structure generation and the behavior pattern of BMECs. The results showed a clear relationship between the BMEC monolayer coverage and the BMEC seeding density. Basically, no hole structure was observed on the model with a low BMEC density, indicating that BMECs in this condition would first elongate and proliferate on the gel surface and not migrate to the inside of the gel. We think it is possible that when there are fewer BMECs, there is enough space on the model surface for their growth to a quantitative threshold, and they would not show the tendency of migration to the gel interior before reaching a point where they can completely cover the model [53]. When many BMECs were seeded, the limited space caused the BMECs to "crowd" each other, inducing their migration to the gel interior and finally forming the hole.

To verify the conjecture about the influence of BMEC migration behavior, the change of BMECs (2×10^5) on the model surface was later clarified by time-lapse experiments. The results shown in Fig. 4 for elastic modulus correspond to our earlier speculation based on the data shown in Fig. 1 and 2 about the relationship between modulus, capillary length, and hole depth. For the low elastic modulus 3D BBB model, the capillary length grows with increasing culture time, and therefore the intensity shows an increasing trend. For the high elastic modulus 3D BBB model, the hole also gradually forms with increasing culture time, and the collapse of the model structure causes a decrease in elastic modulus. On the first day of incubation, a "mountain" of aggregation could be observed on the model surface, and the BMECs still existed as undifferentiated pellets, indicating proliferation and competition among the BMECs. On the third day, the aggregation of BMECs ceased and they converged to form a monolayer, and the morphology changed to a flattened shape after differentiation, probably because BMECs which failed to obtain adhesion space fell off, and the successfully adhered BMECs gradually formed a monolayer after differentiation [53,54].

We also evaluated the role and influence of supporting cells, namely ACs and PCs, in the hole structure formation process. Many studies have shown the existence of cell-cell interaction between ACs, PCs and BMECs, with positive significance for angiogenesis, tight junctions formation and expression of enzymatic systems [55–57]. We have labeled ACs and PCs respectively with CellTracker in our previous studies and demonstrated that ACs and PCs are in close proximity to the BMEC network in the tissue [23,24]. Hole structures were not formed on the model without ACs and BCs inside the gel, which demonstrated that ACs and PCs are important for inducing hole formation in the 3D BBB model [25]. Holes also formed on the model of only ACs and PCs inside and showed the same trend in that hole depth increased with increasing elastic modulus, indicating that the formation of holes occurred by BMEC behavior. Calculations showed that there were fewer holes than in the 3D BBB model with BMECs inside, indicating that hole formation is not limited to surface-to-inside processes, but that there are also BMECs growing from the inside and connecting to surface BMECs to form holes.

We next sought to perform RNA sequencing on the three types of models to understand the molecular processes involved in the hole formation and capillary network formation. In the analysis of GO enrichment terms for Hol compared to Net up-regulated genes, lysosome, ECM organization and proteolysis have high enrichment. This probably shows that cells in the models with a hole structure can more easily secrete factors that can dissolve fibrin and these factors break down the scaffolds during the migration of BMECs. The GO enriched terms in Hol and Net showed substantial cell proliferation compared to BM, suggesting that ACs and PCs play a key regulatory role in BMEC proliferation. We also sought to clarify the mechanism of hole structure formation by analyzing key genes. We found there were no significant differences in transporter genes ABCB1, SLC2A1, and TFRC; tight junction gene TJP1; and

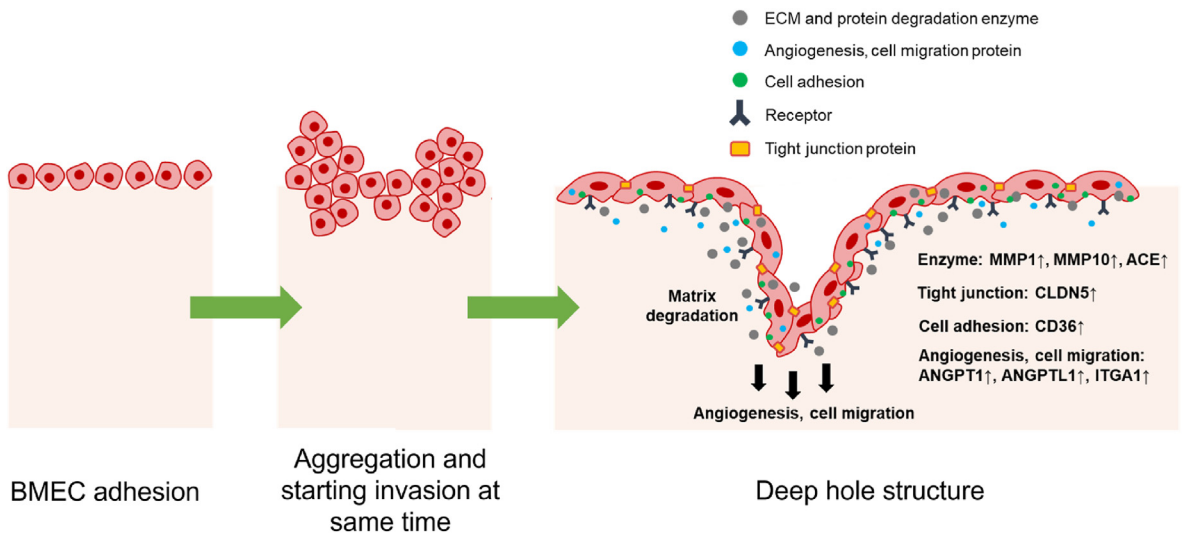

Scheme 2. Schematic illustration of hole structure and capillary network formation in a 3D BBB model on a hard model surface.

endothelial marker PECAM1 (CD31). On the other hand, we found that the gene up-regulated in the Hol model may be related to the hole formation process depicted in Scheme 2. Furthermore, MMP1 and MMP10 have already been shown to have effects on ECM degradation, and ACE is an enzyme gene related to proteolysis [58,59]. Although Fig. 6(d) shows that the MMP1 and MMP10 genes in Hol were down-regulated compared to BM, CD31 marker showed that no hole structures appeared on BM. Therefore, MMP1, MMP10, and ACE genes may lead to the degradation of fibrin gel. Besides, ITGA1, CD36 are proteins involved in cell adhesion; ANGPT1, ANGPTL1, and COL21A1 are proteins involved in angiogenesis processes, so this may explain the simultaneous BMEC migration and hole formation [60–63]. CLDN5 is a gene encoding for Claudin-5, which is a protein related to the high density of the BMEC monolayer and the maintenance of BMEC barrier integrity [64,65]. Frizzled-1 encoded by the FZD1 gene, is a receptor of focal adhesion, collagen, and Wnt signaling pathway proteins [66]. These genes probably collectively guide the cell expression and induce the hole formation.

5. Conclusion

In this study, we regulated the hole and capillary network structure in an *in vitro* 3D BBB model with a special hole structure by adjusting the model elastic modulus. Specifically, we found the hole depth on the bottom surface increased with an increasing elastic modulus of the fibrin gel scaffold, and the internal capillary network length increased with decreasing elastic modulus. Through a series of experiments, we learned that when low numbers of BMECs are seeded on the model bottom surface, they will first perform proliferative behavior and not form holes. The process of hole formation in the 3D BBB model was clarified by time lapse experiments where we found that the BMECs first proliferate, leading to aggregation and invasion when many BMECs are seeded on the model bottom surface, eventually forming a hole. Besides, by adjusting the cell composition in the 3D BBB model, we demonstrated that internal ACs and PCs are important for inducing hole formation on the model surface. From gene expression analysis, we found that the MMP1, MMP10 and ACE genes related to the process of ECM degradation and enzymatic systems, CLDN5 gene related to tight junctions, ANGPT1, ANGPTL1 gene related to angiogenesis, are up-regulated in models with a hole structure and are highly likely to influence the hole formation regulation process. However, there are still some issues in our study, such as we have not demonstrated the functional properties of the BBB model. In the future, we will perform model permeability testing and drug evaluation to improve the model. In conclusion, we demonstrated the possibility of establishing a regulated 3D BBB model and this may provide a new way to fabricate other complex capillary network models by modifying EC types such as human umbilical vein endothelial cells (HUVECs), human lymphatic endothelial cells (HLECs), and human pulmonary microvascular endothelial cells (HPMECs).

Author contributions

YS carried out the experiments. YS and MP wrote and edited the manuscript. MP, JZ, FL, ZX, MM contributed to the design and implementation of the research and to the analysis of the results. All authors have seen and approved the final manuscript.

Declaration of competing interest

The authors declare that they have no known competing financial interests or personal relationships that could have appeared to influence the work reported in this paper.

Data availability

Data will be made available on request.

Acknowledgement

This research was supported by the Institute for JST SPRING (Grant number JPMJSP2138), a Grant-in-Aid for Scientific Research (A) (20H00665), JST-COI NEXT (22–221035869), AMED-MPS2 (22be1004101h0001) and COCKPI-T funding of Takeda Pharmaceutical Company Limited.

Appendix A. Supplementary data

Supplementary data to this article can be found online at https://doi.org/10.1016/j.mtbio.2023.100714.

References

[1] I. Marei, T. Abu Samaan, M.A. Al-Quradaghi, A.A. Farah, S.H. Mahmud, H. Ding, C.R. Triggle, 3D tissue-engineered vascular drug screening platforms: promise and considerations, Front. Cardiovasc. Med. 9 (2022), 847554, https://doi.org/10.3389/fcvm.2022.847554.
[2] F. Pampaloni, E.G. Reynaud, E.H.K. Stelzer, The third dimension bridges the gap between cell culture and live tissue, Nat. Rev. Mol. Cell Biol. 8 (2007) 839–845, https://doi.org/10.1038/nrm2236.
[3] G.A. Truskey, Advancing cardiovascular tissue engineering, F1000Research 5 (2016) 1045, https://doi.org/10.12688/f1000research.8237.1.

[4] D. Hielscher, C. Kaebisch, B.J.V. Braun, K. Gray, E. Tobiasch, Stem cell sources and graft material for vascular tissue engineering, Stem Cell Rev. Rep. 14 (2018) 642–667, https://doi.org/10.1007/s12015-018-9825-x.

[5] C.D. Devillard, C.A. Marquette, Vascular tissue engineering: challenges and requirements for an ideal large scale blood vessel, Front. Bioeng. Biotechnol. 9 (2021), 721843, https://doi.org/10.3389/fbioe.2021.721843.

[6] S.T. Lust, C.M. Shanahan, R.J. Shipley, P. Lamata, E. Gentleman, Design considerations for engineering 3D models to study vascular pathologies in vitro, Acta Biomater. 132 (2021) 114–128, https://doi.org/10.1016/j.actbio.2021.02.031.

[7] D. Baruffaldi, G. Palmara, C. Pirri, F. Frascella, 3D cell culture: recent development in materials with tunable stiffness, ACS Appl. Bio Mater. 4 (2021) 2233–2250, https://doi.org/10.1021/acsabm.0c01472.

[8] M. Vigen, J. Ceccarelli, A.J. Putnam, Protease-sensitive PEG hydrogels regulate vascularization in vitro and in vivo, Macromol. Biosci. 14 (2014) 1368–1379, https://doi.org/10.1002/mabi.201400161.

[9] A. Brown, H. He, E. Trumper, J. Valdez, P. Hammond, L.G. Griffith, Engineering PEG-based hydrogels to foster efficient endothelial network formation in free-swelling and confined microenvironments, Biomaterials 243 (2020), 119921, https://doi.org/10.1016/j.biomaterials.2020.119921.

[10] K. Chwalek, M.V. Tsurkan, U. Freudenberg, C. Werner, Glycosaminoglycan-based hydrogels to modulate heterocellular communication in in vitro angiogenesis models, Sci. Rep. 4 (2014) 4414, https://doi.org/10.1038/srep04414.

[11] Y. Guo, F. Mei, Y. Huang, S. Ma, Y. Wei, X. Zhang, M. Xu, Y. He, B.C. Heng, L. Chen, X. Deng, Matrix stiffness modulates tip cell formation through the p-PXN-Rac1-YAP signaling axis, Bioact. Mater. 7 (2022) 364–376, https://doi.org/10.1016/j.bioactmat.2021.05.033.

[12] Y.-T. Yeh, S.S. Hur, J. Chang, K.-C. Wang, J.-J. Chiu, Y.-S. Li, S. Chien, Matrix stiffness regulates endothelial cell proliferation through septin 9, PLoS One 7 (2012), e46889, https://doi.org/10.1371/journal.pone.0046889.

[13] A. Aazmi, H. Zhou, W. Lv, M. Yu, X. Xu, H. Yang, Y.S. Zhang, L. Ma, vascularizing the brain in vitro, iScience 25 (2022), 104110, https://doi.org/10.1016/j.isci.2022.104110.

[14] N.J. Abbott, Dynamics of CNS barriers: evolution, differentiation, and modulation, Cell. Mol. Neurobiol. 25 (2005) 5–23, https://doi.org/10.1007/s10571-004-1374-y.

[15] M. Campisi, Y. Shin, T. Osaki, C. Hajal, V. Chiono, R.D. Kamm, 3D self-organized microvascular model of the human blood-brain barrier with endothelial cells, pericytes and astrocytes, Biomaterials 180 (2018) 117–129, https://doi.org/10.1016/j.biomaterials.2018.07.014.

[16] Y. Serlin, I. Shelef, B. Knyazer, A. Friedman, Anatomy and physiology of the blood–brain barrier, Semin. Cell Dev. Biol. 38 (2015) 2–6, https://doi.org/10.1016/j.semcdb.2015.01.002.

[17] A. Williams-Medina, M. Deblock, D. Janigro, In vitro models of the blood–brain barrier: tools in translational medicine, Front. Med. Tech. 2 (2021), 623950, https://doi.org/10.3389/fmedt.2020.623950.

[18] W.M. Pardridge, BLOOD-BRAIN barrier drug targeting: the future of brain drug development, Mol. Interv. 3 (2003) 90–105, https://doi.org/10.1124/mi.3.2.90.

[19] W.M. Pardridge, Why is the global CNS pharmaceutical market so under-penetrated? Drug Discov. Today 7 (2002) 5–7, https://doi.org/10.1016/S1359-6446(01)02082-7.

[20] N.J. Abbott, Blood–brain barrier structure and function and the challenges for CNS drug delivery, J. Inherit. Metab. Dis. 36 (2013) 437–449, https://doi.org/10.1007/s10545-013-9608-0.

[21] A.M. Bosworth, H. Kim, K.P. O'Grady, I. Richter, L. Lee, B.J. O'Grady, E.S. Lippmann, Influence of substrate stiffness on barrier function in an iPSC-derived in vitro blood-brain barrier model, Cell. Mol. Bioeng. 15 (2022) 31–42, https://doi.org/10.1007/s12195-021-00706-8.

[22] F. Du, E.V. Shusta, S.P. Palecek, Extracellular matrix proteins in construction and function of in vitro blood-brain barrier models, Front. Chem. Eng. 5 (2023), 1130127, https://doi.org/10.3389/fceng.2023.1130127.

[23] A. Figarol, M. Piantino, T. Furihata, T. Satoh, S. Sugiura, T. Kanamori, M. Matsusaki, Interstitial flow regulates in vitro three-dimensional self-organized brain micro-vessels, Biochem. Biophys. Res. Commun. 533 (2020) 600–606, https://doi.org/10.1016/j.bbrc.2020.09.061.

[24] F. Agathe, N. Yasuhiro, S.-M. Yukari, F. Tomomi, S. Kaoru, M. Matsusaki, An in vitro self-organized three-dimensional model of the blood-brain barrier microvasculature, Biomed. Mater. 16 (2021), 015006, https://doi.org/10.1088/1748-605X/aba5f1.

[25] M. Piantino, D.-H. Kang, T. Furihata, N. Nakatani, K. Kitamura, Y. Shigemoto-Mogami, K. Sato, M. Matsusaki, Development of a three-dimensional blood-brain barrier network with opening capillary structures for drug transport screening assays, Mater. Today Bio. 15 (2022), 100324, https://doi.org/10.1016/j.mtbio.2022.100324.

[26] B.A. Juliar, M.T. Keating, Y.P. Kong, E.L. Botvinick, A.J. Putnam, Sprouting angiogenesis induces significant mechanical heterogeneities and ECM stiffening across length scales in fibrin hydrogels, Biomaterials 162 (2018) 99–108, https://doi.org/10.1016/j.biomaterials.2018.02.012.

[27] N. Salam, S. Toumpaniari, P. Gentile, A. Marina Ferreira, K. Dalgarno, S. Partridge, Assessment of migration of human MSCs through fibrin hydrogels as a tool for formulation optimisation, Materials 11 (2018) 1781, https://doi.org/10.3390/ma11091781.

[28] M. Keating, M. Lim, Q. Hu, E. Botvinick, Selective stiffening of fibrin hydrogels with micron resolution via photocrosslinking, Acta Biomater. 87 (2019) 88–96, https://doi.org/10.1016/j.actbio.2019.01.034.

[29] R. Ito, K. Umehara, S. Suzuki, K. Kitamura, K. Nunoya, Y. Yamaura, H. Imawaka, S. Izumi, N. Wakayama, T. Komori, N. Anzai, H. Akita, T. Furihata, A human immortalized cell-based blood–brain barrier triculture model: development and characterization as a promising tool for Drug−Brain permeability studies, Mol. Pharm. 16 (2019) 4461–4471, https://doi.org/10.1021/acs.molpharmaceut.9b00519.

[30] T. Furihata, R. Ito, A. Kamiichi, K. Saito, K. Chiba, Establishment and characterization of a new conditionally immortalized human astrocyte cell line, J. Neurochem. 136 (2016) 92–105, https://doi.org/10.1111/jnc.13358.

[31] K. Umehara, Y. Sun, S. Hiura, K. Hamada, M. Itoh, K. Kitamura, M. Oshima, A. Iwama, K. Saito, N. Anzai, K. Chiba, H. Akita, T. Furihata, A new conditionally immortalized human fetal brain pericyte cell line: establishment and functional characterization as a promising tool for human brain pericyte studies, Mol. Neurobiol. 55 (2018) 5993–6006, https://doi.org/10.1007/s12035-017-0815-9.

[32] T. Quach, M. Tippens, F. Szlam, R. Van Dyke, J.H. Levy, M. Csete, Quantitative assessment of fibrinogen cross-linking by ?aminocaproic acid in patients with end-stage liver disease, Liver Transplant. 10 (2004) 123–128, https://doi.org/10.1002/lt.20011.

[33] J. Schindelin, I. Arganda-Carreras, E. Frise, V. Kaynig, M. Longair, T. Pietzsch, S. Preibisch, C. Rueden, S. Saalfeld, B. Schmid, J.-Y. Tinevez, D.J. White, V. Hartenstein, K. Eliceiri, P. Tomancak, A. Cardona, Fiji: an open-source platform for biological-image analysis, Nat. Methods 9 (2012) 676–682, https://doi.org/10.1038/nmeth.2019.

[34] D. Torre, A. Lachmann, A. Ma'ayan, BioJupies: automated generation of interactive notebooks for RNA-seq data analysis in the cloud, Cell Sys. 7 (2018) 556–561.e3, https://doi.org/10.1016/j.cels.2018.10.007.

[35] I. Inza, P. Larrañaga, R. Blanco, A.J. Cerrolaza, Filter versus wrapper gene selection approaches in DNA microarray domains, Artif. Intell. Med. 31 (2004) 91–103, https://doi.org/10.1016/j.artmed.2004.01.007.

[36] P.A. Mundra, J.C. Rajapakse, Gene and sample selection using T-score with sample selection, J. Biomed. Inf. 59 (2016) 31–41, https://doi.org/10.1016/j.jbi.2015.11.003.

[37] C.M. Ghajar, X. Chen, J.W. Harris, V. Suresh, C.C.W. Hughes, N.L. Jeon, A.J. Putnam, S.C. George, The effect of matrix density on the regulation of 3-D capillary morphogenesis, Biophys. J. 94 (2008) 1930–1941, https://doi.org/10.1529/biophysj.107.120774.

[38] J.J. Moon, J.E. Saik, R.A. Poché, J.E. Leslie-Barbick, S.-H. Lee, A.A. Smith, M.E. Dickinson, J.L. West, Biomimetic hydrogels with pro-angiogenic properties, Biomaterials 31 (2010) 3840–3847, https://doi.org/10.1016/j.biomaterials.2010.01.104.

[39] J.I. Alvarez, T. Katayama, A. Prat, Glial influence on the blood brain barrier, Glia 61 (2013) 1939, https://doi.org/10.1002/glia.22575. –1958.

[40] F. De Smet, I. Segura, K. De Bock, P.J. Hohensinner, P. Carmeliet, Mechanisms of vessel branching: filopodia on endothelial tip cells lead the way, Arterioscler. Thromb. Vasc. Biol. 29 (2009) 639–649, https://doi.org/10.1161/ATVBAHA.109.185165.

[41] S. Kim, H. Lee, M. Chung, N.L. Jeon, Engineering of functional, perfusable 3D microvascular networks on a chip, Lab Chip 13 (2013) 1489, https://doi.org/10.1039/c3lc41320a.

[42] M.W. Tibbitt, K.S. Anseth, Hydrogels as extracellular matrix mimics for 3D cell culture, Biotechnol. Bioeng. 103 (2009) 655–663, https://doi.org/10.1002/bit.22361.

[43] S.R. Caliari, J.A. Burdick, A practical guide to hydrogels for cell culture, Nat. Methods 13 (2016) 405–414, https://doi.org/10.1038/nmeth.3839.

[44] G. Charras, E. Sahai, Physical influences of the extracellular environment on cell migration, Nat. Rev. Mol. Cell Biol. 15 (2014) 813–824, https://doi.org/10.1038/nrm3897.

[45] S. van Helvert, C. Storm, P. Friedl, Mechanoreciprocity in cell migration, Nat. Cell Biol. 20 (2018) 8–20, https://doi.org/10.1038/s41556-017-0012-0.

[46] S. Budday, R. Nay, R. de Rooij, P. Steinmann, T. Wyrobek, T.C. Ovaert, E. Kuhl, Mechanical properties of gray and white matter brain tissue by indentation, J. Mech. Behav. Biomed. Mater. 46 (2015) 318–330, https://doi.org/10.1016/j.jmbbm.2015.02.024.

[47] H. Duong, B. Wu, B. Tawil, Modulation of 3D fibrin matrix stiffness by intrinsic fibrinogen–thrombin compositions and by extrinsic cellular activity, Tissue Eng. 15 (2009) 1865–1876, https://doi.org/10.1089/ten.tea.2008.0319.

[48] T. Luo, B. Tan, L. Zhu, Y. Wang, J. Liao, A review on the design of hydrogels with different stiffness and their effects on tissue repair, Front. Bioeng. Biotechnol. 10 (2022), 817391, https://doi.org/10.3389/fbioe.2022.817391.

[49] Y. Duan, X. Li, X. Zuo, T. Shen, S. Yu, L. Deng, C. Gao, Migration of endothelial cells and mesenchymal stem cells into hyaluronic acid hydrogels with different moduli under induction of pro-inflammatory macrophages, J. Mater. Chem. B 7 (2019) 5478–5489, https://doi.org/10.1039/C9TB01126A.

[50] M. Jiroušková, J.K. Jaiswal, B.S. Coller, Ligand density dramatically affects integrin αIIbβ3-mediated platelet signaling and spreading, Blood 109 (2007) 5260–5269, https://doi.org/10.1182/blood-2006-10-054015.

[51] Y.K. Kumar, D.D.S. Lohchab, Influence of aviation fuel on mechanical properties of glass fiber-reinforced plastic composite, IARJSET 3 (2016).

[52] N. Annabi, S.M. Mithieux, E.A. Boughton, A.J. Ruys, A.S. Weiss, F. Dehghani, Synthesis of highly porous crosslinked elastin hydrogels and their interaction with fibroblasts in vitro, Biomaterials 30 (2009) 4550–4557, https://doi.org/10.1016/j.biomaterials.2009.05.014.

[53] E. Montañez, Comparative study of tube assembly in three-dimensional collagen matrix and on Matrigel coats, Angiogenesis 5 (2002) 167–172, https://doi.org/10.1023/A:1023837821062.

[54] E.H. Nguyen, W.T. Daly, N.N.T. Le, M. Farnoodian, D.G. Belair, M.P. Schwartz, C.S. Lebakken, G.E. Ananiev, M.A. Saghiri, T.B. Knudsen, N. Sheibani, W.L. Murphy, Versatile synthetic alternatives to Matrigel for vascular toxicity screening and stem cell expansion, Nat. Biomed. Eng. 1 (2017) 96, https://doi.org/10.1038/s41551-017-0096.

[55] D. Bonkowski, V. Katyshev, R.D. Balabanov, A. Borisov, P. Dore-Duffy, The CNS microvascular pericyte: pericyte-astrocyte crosstalk in the regulation of tissue survival, Fluids Barriers CNS 8 (2011) 8, https://doi.org/10.1186/2045-8118-8-8.

[56] D.H. Jo, J.H. Kim, J.-I. Heo, J.H. Kim, C.-H. Cho, Interaction between pericytes and endothelial cells leads to formation of tight junction in hyaloid vessels, Mol. Cell. 36 (2013) 465–471, https://doi.org/10.1007/s10059-013-0228-1.

[57] T. Zidarič, L. Gradišnik, T. Velnar, Astrocytes and human artificial blood-brain barrier models, Bosn. J. Basic Med. Sci. (2022), https://doi.org/10.17305/bjbms.2021.6943.

[58] V. Beldent, A. Michaud, L. Wei, M.T. Chauvet, P. Corvol, Proteolytic release of human angiotensin-converting enzyme. Localization of the cleavage site, J. Biol. Chem. 268 (1993) 26428–26434, https://doi.org/10.1016/S0021-9258(19)74332-4.

[59] W.B. Saunders, K.J. Bayless, G.E. Davis, MMP-1 activation by serine proteases and MMP-10 induces human capillary tubular network collapse and regression in 3D collagen matrices, J. Cell Sci. 118 (2005) 2325–2340, https://doi.org/10.1242/jcs.02360.

[60] K.C. Ehrlich, M. Lacey, M. Ehrlich, Tissue-specific epigenetics of atherosclerosis-related ANGPT and ANGPTL genes, Epigenomics 11 (2019) 169–186, https://doi.org/10.2217/epi-2018-0150.

[61] M.-Y. Chou, H.-C. Li, Genomic organization and characterization of the human type XXI collagen (COL21A1) gene, Genomics 79 (2002) 395–401, https://doi.org/10.1006/geno.2002.6712.

[62] H.Y. Huh, S.K. Lo, L.M. Yesner, R.L. Silverstein, CD36 induction on human monocytes upon adhesion to tumor necrosis factor-activated endothelial cells, J. Biol. Chem. 270 (1995) 6267–6271, https://doi.org/10.1074/jbc.270.11.6267.

[63] D. Xu, T. Li, R. Wang, R. Mu, Expression and pathogenic analysis of integrin family genes in systemic sclerosis, Front. Med. 8 (2021), 674523, https://doi.org/10.3389/fmed.2021.674523.

[64] K.J. Hewitt, R. Agarwal, P.J. Morin, The claudin gene family: expression in normal and neoplastic tissues, BMC Cancer 6 (2006) 186, https://doi.org/10.1186/1471-2407-6-186.

[65] C. Greene, N. Hanley, M. Campbell, Claudin-5: gatekeeper of neurological function, Fluids Barriers CNS 16 (2019) 3, https://doi.org/10.1186/s12987-019-0123-z.

[66] C. Bonnet, A. Brahmbhatt, S.X. Deng, J.J. Zheng, Wnt signaling activation: targets and therapeutic opportunities for stem cell therapy and regenerative medicine, RSC Chem. Biol. 2 (2021) 1144–1157, https://doi.org/10.1039/D1CB00063B.